Inorganic Chemistry

pubs.acs.org/IC Article

# Tuning Magnetic Interactions Between Triphenylene Radicals by Variation of Crystal Packing in Structures with Alkali Metal Counterions

Zheng Zhou, Ökten Üngör, Zheng Wei, Michael Shatruk,* Alexandra Tsybizova, Renana Gershoni-Poranne,* and Marina A. Petrukhina*

Cite This: *Inorg. Chem.* 2021, 60, 14844−14853 Read Online

ACCESS | Metrics & More | Article Recommendations | Supporting Information

**ABSTRACT:** The monoanion of triphenylene ($C_{18}H_{12}$, **1**) was generated in THF using several alkali metals (Na, K, Rb, and Cs) as reducing agents and crystallized with the corresponding cations in the presence of 18-crown-6 ether. The UV−vis spectroscopy points to the metal-dependent coordination environment of the triphenylene monoanion-radicals, $\mathbf{1}^{\cdot-}$, in solution. The X-ray diffraction characterization confirmed the formation of a solvent-separated ion pair (SSIP) with sodium ions, $[\{Na^+(18\text{-crown-}6)(THF)_2\}(\mathbf{1}^{\cdot-})]$ (**2**), and three contact-ion pair (CIP) complexes formed by larger alkali metal ions, $[\{K^+(18\text{-crown-}6)\}(\mathbf{1}^{\cdot-})]$ (**3**), $[\{Rb^+(18\text{-crown-}6)\}(\mathbf{1}^{\cdot-})]$ (**4**), and $[\{Cs^+(18\text{-crown-}6)\}(\mathbf{1}^{\cdot-})]$ (**5**). Structural analysis of the series reveals a notable geometry perturbation of the triphenylene framework in **2** caused by one-electron acquisition, which is further enhanced by direct metal binding in **3**−**5**. This has been correlated with the aromaticity changes and charge redistribution upon one-electron reduction of **1**, as revealed by the computational studies. The EPR spectroscopy and magnetic susceptibility measurements confirm antiferromagnetic interactions corresponding to an $S = 1/2$ system in the solid state. The magnetic behavior of **3**−**5** correlates with the arrangement of triphenylene radicals in the crystal structures. All three compounds exhibit antiferromagnetic (AFM) interactions between $S = 1/2$ radicals in the solid state, but the exchange coupling in **4** and **5** is notably stronger than that in **3**, which leads to AFM ordering at 3.8 K in **4** and at 2.0 K in **5**. The magnetic phase transitions in **4** and **5** can be interpreted as originating from interactions between the chains of the AFM-coupled $S = 1/2$ radicals.

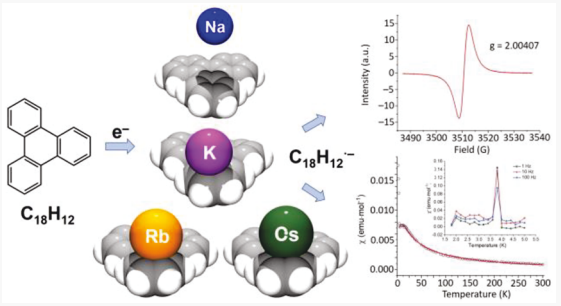


## INTRODUCTION

The reduction of polycyclic aromatic hydrocarbons (PAHs) attracts significant attention from fundamental and applied viewpoints.[1−6] Chemical reduction of PAHs with alkali metals yields negatively charged $\pi$-conjugated carbanions which may undergo structural changes[7−19] and core transformation,[20−22] in addition to reductive dimerization processes.[23−26] These reactions also afford new solid materials with intriguing electronic,[27−29] conducting,[30−36] and magnetic properties.[37,38] However, an in-depth understanding of materials properties and structure−property correlations is often impeded by the lack of pure single-crystalline phases. For example, the chemical reduction of triphenylene ($C_{18}H_{12}$, **1**) was first reported by Paul et al. back in 1956,[39] revealing a notable color change upon reaction of **1** with alkali metals in THF. During the following decades, reduction processes of triphenylene have been broadly studied in solution by UV−vis and IR spectroscopy[40−43] and electrochemistry.[44−46] Due to $D_{3h}$ symmetry, the HOMO and LUMO of **1** are doubly degenerate, allowing a potential triplet ground state upon a 2-fold reduction.[47] This attracted significant attention of the scientific community to investigation of the reduction processes of **1** by EPR spectroscopy.[41,48,49] The EPR study of mono- and doubly-reduced triphenylene was first reported by the Boer group in 1967, confirming that both exhibit radical behavior.[48] It was also found that the spectral resolution of the monoanion $\mathbf{1}^{\cdot-}$ generated by the Na-induced reduction is affected by temperature and coordinating solvents. Several years later, the Freed group reported the EPR study of the Li-induced reduction of **1** in DME, revealing similar results to those obtained with Na metal.[49] However, all earlier works have been focused on solution behavior of *in situ* generated triphenylene monoanion-radicals that could not reveal geometry perturbation or specific coordination environment of $\mathbf{1}^{\cdot-}$. In 2001, Lemaire et al. prepared a series of microcrystalline triphenylide-based samples and found that only the potassium

Received: July 14, 2021
Published: September 15, 2021

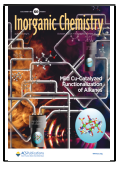

Downloaded via FLORIDA STATE UNIV on October 7, 2021 at 16:19:30 (UTC).
See https://pubs.acs.org/sharingguidelines for options on how to legitimately share published articles.

ACS Publications © 2021 American Chemical Society



https://doi.org/10.1021/acs.inorgchem.1c02139
*Inorg. Chem.* 2021, 60, 14844−14853

salt exhibits the semiconductor-like properties.[41] Recently, Štefančic et al. reported the first X-ray structure characterization of the monoreduced triphenylene crystallized from DME as $[\{K^+_2(DME)\}(\mathbf{1}^{\cdot-})_2]_\infty$.[50] The magnetic measurement of the crystalline material was complemented by EPR spectroscopy study, revealing a sharp and strong signal at $g$ = 2.0028 at 100 K in the X-band EPR spectrum. As the temperature cools down to 4 K, the sharp signal disappears, and an anisotropic signal dominates the EPR spectrum instead.[50] The EPR spectroscopy and magnetic studies of this solid revealed it is a Mott insulator with strong antiferromagnetic exchange interactions. The 3D solid-state packing of the electronically active triphenylide anions with potassium countercations could be responsible for a surprisingly strong antiferromagnetic exchange. These intriguing results should have triggered a broad investigation of the triphenylide-based solids isolated under different experimental conditions and/or with other alkali metals, but no further studies have followed.

In this work, we set out to explore the chemical reduction behavior of triphenylene using several different alkali metals, namely, sodium (Na), potassium (K), rubidium (Rb), and cesium (Cs). Since cation-$\pi$ interactions could be effectively used in modulating the solid-state packing, we targeted the isolation of single-crystalline materials for a comprehensive structure/property correlation study. We successfully accomplished the synthesis, crystallization, and characterization of four new alkali metal salts of the monoreduced triphenylene using X-ray diffraction, magnetic measurements, and spectroscopic techniques. We revealed antiferromagnetic (AFM) ordering in the Rb- and Cs-containing complexes due to exchange interactions between zigzag chains of AFM-coupled triphenylene radicals in the solid state.

## RESULTS AND DISCUSSION

**Crystallographic Study of Monoreduced Triphenylene Products.** The crystal structure of triphenylene ($C_{18}H_{12}$, **1**) was first reported by Ahmed in 1963,[51] and it was optimized by Prasad in 2014.[52] Since the only prior example of the crystallographically characterized triphenylide-based molecular solid pointed to the importance of cation-$\pi$ interactions,[50] we explored the effect of different alkali metals on tuning the solid-state structures and properties of the resulting products.

Chemical reduction reactions of **1** with four alkali metals ranging from Na to Cs were performed at room temperature in THF in the presence of 18-crown-6 ether (Scheme 1). These reactions are accompanied by the appearance of a dark violet color, which had been previously assigned to the monoreduced form of **1** by Paul[39] and Arick.[40] By slow diffusion of hexanes into the THF reaction solutions, four new products of the monoreduced triphenylene, $\mathbf{1}^{\cdot-}$, have been crystallized with different alkali metal counterions. The X-ray diffraction analysis revealed the formation of a solvent-separated ion pair, $[\{Na^+(18\text{-crown-6})(THF)_2\}(\mathbf{1}^{\cdot-})]$ (**2**), and three contact-ion pair complexes, $[\{K^+(18\text{-crown-6})\}(\mathbf{1}^{\cdot-})]_\infty$ (**3**), $[\{Rb^+(18\text{-crown-6})\}(\mathbf{1}^{\cdot-})]$ (**4**), and $[\{Cs^+(18\text{-crown-6})\}(\mathbf{1}^{\cdot-})]$ (**5**). Phase purity of the bulk crystalline samples was confirmed by X-ray powder diffraction (Figures S10–S13, Tables S1–S4).

The UV–vis spectra of crystals **2**–**5** dissolved in THF are consistent with the data reported previously.[40] Notably, the four absorption maxima in the UV–vis spectrum of **5** are notably shifted in comparison to those in **2** (Figure 1), reflecting the effect of metal counterions in the series. At the same time, the UV–vis spectra of two close analogues, **4** and **5**, are very similar.

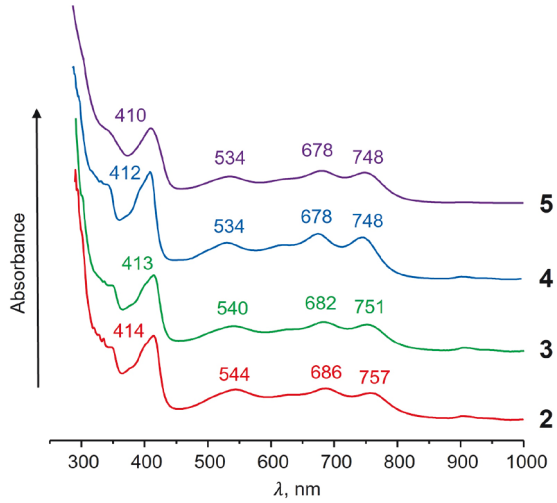


**Figure 1.** UV–vis spectra of **2**–**5** in THF.

In the crystal structure of **2** (Figure 2a,b), the $Na^+$ ion is wrapped by one 18-crown-6 ether and two THF molecules and

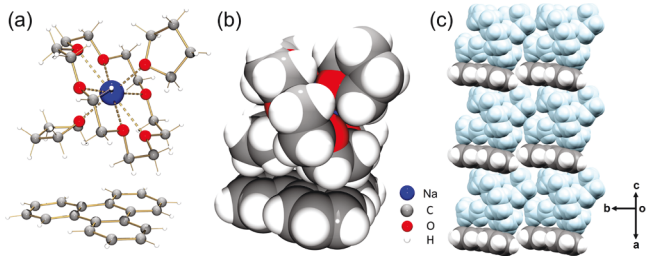


**Figure 2.** Crystal structure of $[\{Na^+(18\text{-crown-6})(THF)_2\}(\mathbf{1}^{\cdot-})]$ (**2**): (a) ball-and-stick and (b) space-filling models, (c) solid-state packing, space-filling model.

is fully isolated from the triphenylene surface, thus providing the first example of a "naked" monoanion for $\mathbf{1}^{\cdot-}$. In the cationic moiety, both the $Na\cdots O_{crown}$ (2.610(4)–2.845(4) Å) and $Na\cdots O_{THF}$ distances (2.259(4) and 2.266(12) Å) are close to those previously reported.[16−19,53,54] In the solid-state structure of **2** (Figure 2c), the 1D columns are formed through weak C–H$\cdots\pi$ interactions between the surface of $\mathbf{1}^{\cdot-}$ anions and $\{Na^+(18\text{-crown-6})(THF)_2\}$ cations, with the distances ranging over 2.479(7)–2.728(7) Å. There are no interactions found between the adjacent 1D columns.

In contrast to **2**, the crystallographic characterization of **3** (Figure 3a,b) reveals a contact-ion pair complex. The $K^+$ ion is

**Scheme 1. Chemical Reduction of 1**

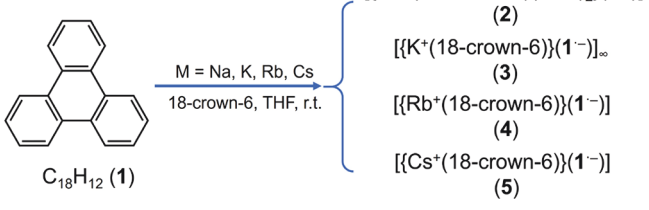



https://doi.org/10.1021/acs.inorgchem.1c02139
Inorg. Chem. 2021, 60, 14844–14853

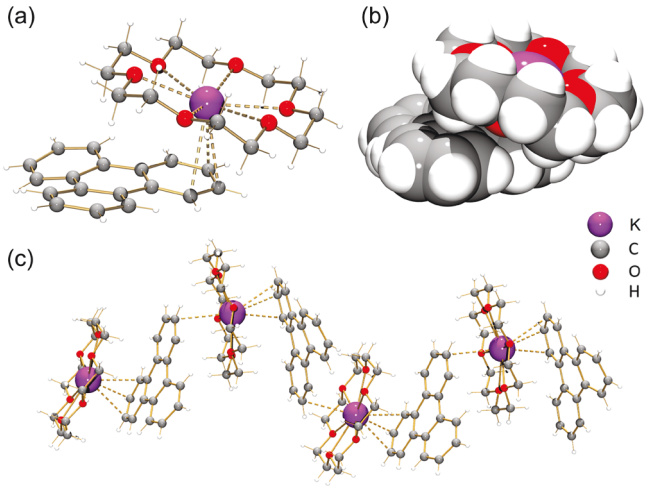


**Figure 3.** Crystal structure of $[\{K^+(18\text{-crown-6})\}(\mathbf{1}^{\cdot-})]_\infty$ (**3**): (a) ball-and-stick and (b) space-filling models, (c) 1D polymeric chain, ball-and-stick model.

bound to one of the peripheral six-membered rings of $\mathbf{1}^{\cdot-}$ in a $\eta^3$-mode, with the shortest K···C distances of 3.151(4) Å–3.262(4) Å (see Figure S19 for more details). The $K^+$ ion is also trapped by one 18-crown-6 ether with the K···$O_{crown}$ distances ranging over 2.736(12)–2.892(12) Å. The $\{K^+(18\text{-crown-6})\}$ moiety is tilted at 12.6° in respect to the $\pi$-surface of $\mathbf{1}^{\cdot-}$. All K···C and K···O distances are comparable to those found in the literature.[17,19,50,53] One additional longer K···C contact (3.407(4) Å) is found to the adjacent $\mathbf{1}^{\cdot-}$ anion, resulting in the propagation of a 1D polymeric chain in **3** (Figure 3c). This 1D arrangement contrasts the only previously reported $[\{K^+_2(DME)\}(\mathbf{1}^{\cdot-})_2]_\infty$ structure,[50] in which multiple $K^+$ ions bind to the triphenylene surface from both sides, forming an extended 3D network based on cation-$\pi$ interactions. In the solid-state structure of **3**, the 1D polymeric chains are further packed into a 2D layer through C–H···$\pi$ interactions (2.587(3)–2.737(3) Å) between $\mathbf{1}^{\cdot-}$ and $\{K^+(18\text{-crown-6})\}$ moieties from the adjacent columns.

In the crystal structure of **4** (Figure 4), the $Rb^+$ ion is coordinated to a peripheral six-membered ring of $\mathbf{1}^{\cdot-}$ in a $\eta^6$-

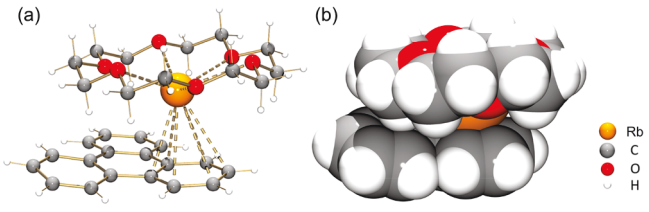


**Figure 4.** Crystal structure of $[\{Rb^+(18\text{-crown-6})\}(\mathbf{1}^{\cdot-})]$ (**4**): (a) ball-and-stick and (b) space-filling models.

mode, with the Rb···C distances ranging over 3.191(3)–3.645(3) Å (see Figure S20 for more details). The $Rb^+$ ion is also wrapped by one 18-crown-6 ether molecule (Rb···$O_{crown}$: 2.856(2)–3.107(2) Å), with all distances being close to the reported values.[16,54] As **4** and **5** are isostructural, similar metal ion coordination is observed in the crystal structure of the $Cs^+$ analogue with the Cs···C and Cs···$O_{crown}$ distances of 3.257(1)–3.761(1) Å and 2.972(1)–3.255(1) Å, respectively (Figures S18 and S21). A more parallel alignment of the $\{Rb^+(18\text{-crown-6})\}$ moiety toward the surface of $\mathbf{1}^{\cdot-}$ is observed in **4**, with the tilt angle decreased to 4.2° vs 12.6° in **3** and 8.9° in **5**. Owing to their large ionic size, the $Rb^+$ and $Cs^+$ cations do not fit inside the crown ether cavity and are pulled toward the $\pi$-surface of $\mathbf{1}^{\cdot-}$. A similar effect has been previously seen in the complex of $\{Rb^+(18\text{-crown-6})\}$ with the monoreduced coronene.[54] The full entrapment of the $Rb^+$ or $Cs^+$ ions prevents additional cation-$\pi$ contacts with the adjacent moieties in the solid-state structures of **4** and **5**. However, the propagation of 1D columns occurs through C–H···$\pi$ interactions between the $\mathbf{1}^{\cdot-}$ and $\{M^+(18\text{-crown-6})\}$ moieties that range over 2.486(4)–2.684(4) Å (Figure 5b)

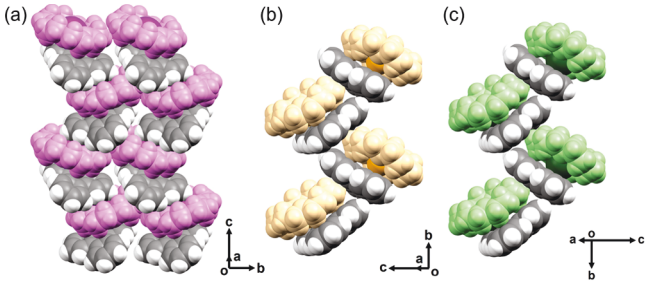


**Figure 5.** Solid-state packing in (a) **3**, (b) **4**, and (c) **5**, space-filling models.

and 2.474(3)–2.698(3) Å (Figure 5c) in **4** and **5**, respectively. Within the columns, large tilting angles of 66.0° and 70.5° with extra slip distances of 6.73 and 7.35 Å are observed in **4** and **5** (Figure S22). In contrast to **3**, the intercolumn contacts between the adjacent radicals $\mathbf{1}^{\cdot-}$ are found in the solid-state structures of **4** (2.759(4) and 3.026(4) Å, Figure S23) and 5 (2.749(3) and 3.001(3) Å, Figure S24).

The set of structurally characterized complexes ranging from a "naked" radical-anion $\mathbf{1}^{\cdot-}$ in **2** to the complexed anions in **3**–**5** enables analysis of the consequences of the reduction and metal binding for triphenylene. Specifically, the addition of one electron to **1** results in the deformation of the polyaromatic core, which can be evaluated by comparison of dihedral angles (Table 1) and least-squares-plane calculations. According to the planarity evaluation (Table S6), the central six-membered ring experiences the most distortion in both neutral and monoreduced forms of triphenylene. For the parent **1**, the carbon framework is almost planar with the average dihedral

**Table 1. Dihedral Angles (deg) in 1–5, along with a Labeling Scheme**

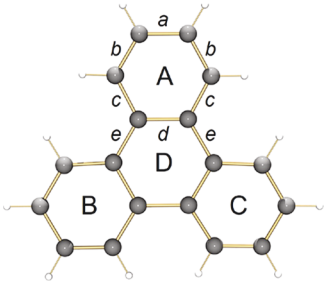


| | 1[52] | 2 | 3 | 4 | 5 |
|---|---|---|---|---|---|
| A/D | 2.2 | 2.6 | 7.2 | 6.4 | 7.1 |
| B/D | 1.3 | 5.1 | 10.6 | 3.9 | 4.1 |
| C/D | 2.4 | 3.9 | 8.5 | 6.5 | 5.8 |

[a]The ring involved in metal ion coordination is labeled as A.



https://doi.org/10.1021/acs.inorgchem.1c02139
Inorg. Chem. 2021, 60, 14844–14853

angle of 2.0°, but it bends slightly in the "naked" monoanion (avg. 3.9°) in **2**. With the addition of metal ion binding, the core of $\mathbf{1}^{\cdot-}$ bends slightly more in the contact-ion pair complexes **4** and **5** (avg. 5.6° in both). Notably, coordination of two $K^+$ ions to the opposite sides of $\mathbf{1}^{\cdot-}$ in an asymmetric fashion (Figure 4) results in additional bending with the average dihedral angle of 8.8° in **3**. These structural changes upon one-electron reduction of **1** have not been seen in the previously reported structure,[50] where binding of four $K^+$ ions to both sides of $\mathbf{1}^{\cdot-}$ may have prevented the carbon framework from bending (avg. 2.4°).

In neutral **1**, the C−C bond distances at position ***e*** are 1.464(5)−1.470(5) Å.[52] Notably, one of the bonds of $\mathbf{1}^{\cdot-}$ at position ***e*** is shortened by about 0.03 Å (1.435(7) Å) in **2** and it is further reduced in the CIP complexes **3**−**5** (1.416(3) Å, 1.416(4) Å, 1.425(4) Å, respectively). As also observed in $[\{K^+_2(DME)\}(\mathbf{1}^{\cdot-})_2]_\infty$,[50] this may be a general indication of the increased electronic density around the specific area of the monoreduced triphenylene core (Table 2).

**Table 2. Selected C−C Bond Length Distances (Å) of $\mathbf{1}^{\cdot-}$ in 1−5**

| | $\mathbf{1}$[52] | **2** | **3** | **4** | **5** |
|---|---|---|---|---|---|
| **a** | 1.376(5) −1.385(5) | 1.386(7) −.403(7) | 1.388(4) −.391(5) | 1.396(5) −1.398(4) | 1.399(3) −1.405(3) |
| **b** | 1.376(5) −1.384(5) | 1.363(7) −.375(7) | 1.381(4) −1.416(4) | 1.372(5) −1.404(5) | 1.378(3) −1.402(3) |
| **c** | 1.404(5) −1.416(5) | 1.403(7) −.426(7) | 1.402(3) −.458(3) | 1.394(4) −1.442(4) | 1.400(3) −1.442(3) |
| **d** | 1.405(5) −1.411(5) | 1.418(7) −.433(7) | 1.415(3) −.440(3) | 1.416(4) −.447(4) | 1.418(3) −1.443(3) |
| ***e*** | 1.464(5) −1.470(5) | 1.435(7) −.459(6) | 1.416(3) −.460(3) | 1.416(4) −.469(4) | 1.425(3) −1.469(3) |

**DFT Results and Discussion.** In order to better understand the behavior of the triphenylene radical-anion, $\mathbf{1}^{\cdot-}$, and its binding to $K^+$, $Rb^+$, and $Cs^+$ cations, we performed a computational investigation, studying the geometrical, electronic, and aromatic changes the system undergoes upon addition of one electron and subsequently upon complexation to the crown-ether stabilized alkali metal ion.

The neutral triphenylene optimizes to a planar, $D_{3h}$-symmetric system. The electrostatic potential (ESP) map shows delocalization on the entire face of the polycyclic system (Figure 6a) and the system displays aromatic character, as measured by the nucleus independent chemical shift (NICS) method.[55−57] For the $\pi$-complexes, the NICS probes were placed above the face of the triphenylene that is opposite of the complexed metal ion, to avoid any undesired effects from the metal center. For the neutral parent, $\sum NICS(1.7)_{ZZ} = -74$ ppm (calculated as the sum of values measured above the centers of the individual six-membered rings, $NICS(1.7)_{ZZ} = -20, -14$ ppm for the side and center rings, respectively, Figure 6a), which is indicative of the diatropic ring currents and the aromatic nature of the system.

Upon addition of an electron to form the radical-anion $\mathbf{1}^{\cdot-}$, the system becomes antiaromatic and undergoes a second-order Jahn−Teller distortion, reducing its symmetry to $C_{2v}$. This change in symmetry is reflected in the partial charges (Figure 6b), which show that the charge is accumulated on the central ring (ring D, charge = −0.728) and two of the side rings (rings B and C, charge = −0.374) rather than being evenly distributed. The NICS values also reflect the reduction in symmetry: $NICS(1.7)_{ZZ}$ = 28, 40, and 50 ppm, for rings A, B/C, and D, respectively. In addition, a correspondence between the increase in NICS value and the magnitude of the charge can be noted. The link between charge and paratropicity is not surprising, as both share a common molecular orbital basis.[58,59]

Notably, the ESP maps (Figure 6) show the distribution at only one isosurface value and do not reflect the total charges. For this reason, the sums of partial charges of the individual six-membered rings were used as a more reliable reflection of the charge distribution of the $\mathbf{1}^{\cdot-}$ system. Overall, one can perceive the electronic behavior of the triphenylene radical-anion as a balancing act between the stabilizing effect of charge delocalization and the destabilizing effect of antiaromaticity, whereby the cost of localizing the charge on a smaller portion of the structure is apparently mitigated by reducing the antiaromaticity of one of the side rings.

This approach has been extended to the analysis of alkali metal ion complexation by triphenylene radical-anion. As a first estimation, one can consider the total NICS values as an indication of the metal-complexation effect on the aromaticity in the system. For the bare radical-anion, $\sum NICS(1.7)_{ZZ}$ = 158 ppm, while for the potassium(I), rubidium(I), and cesium(I) $\pi$-complexes, the $\sum NICS(1.7)_{ZZ}$ values are 92, 104, and 122 ppm, respectively, indicating that the complexation has a stabilizing effect of reducing the antiaromatic character of $\mathbf{1}^{\cdot-}$. This is achieved due to the Coulombic attraction between the $\mathbf{1}^{\cdot-}$ anion and the respective cation, alleviating part of the negative charge on the triphenylene unit, as can be seen from the charges on $\mathbf{1}^{\cdot-}$ in the potassium(I), rubidium(I), and cesium(I) complexes (total charge = −0.829, −0.866, and −0.989, respectively, compared to −1 for the uncomplexed $\mathbf{1}^{\cdot-}$).

Not surprisingly, even though the crystal structures show that the metal ions interact with one side-ring only, ring C (Figure 6), the entire $\pi$-system of $\mathbf{1}^{\cdot-}$ is affected. The electrostatic interaction with the metal exacerbates the polarization, as observed in the partial charges and ESP maps (Figure 6c−e), reducing the charge on ring A (and to a lesser extent also on ring B) and increasing it on rings C and D. We find that the partial charges are linearly correlated to the paratropic (i.e., antiaromatic) character, as assessed with the NICS metric (Figure S25), which supports our hypothesis that the alleviation of charge stabilizes the system via relief of antiaromaticity. Comparison between the three complexes suggests that, as the metal cation size increases, the polarization of the triphenylene becomes more pronounced but the charge transfer decreases. Accordingly, complexation to the $K^+$ ion has the least polarizing effect but the strongest charge transfer. The larger metals, $Rb^+$ and $Cs^+$, create a more pronounced polarization in the $\pi$-system but are less successful at alleviating the total charge of the triphenylene. This is perhaps attributed to the larger size of the $Rb^+$ and $Cs^+$ ions having more diffuse positive charge, which reduces their Coulombic interactions with the $\pi$-surface of $\mathbf{1}^{\cdot-}$. These results are in line with the report by Stanger which shows that the aromaticity of benzene in the $(benzene)Cr(CO)_3$ complex is reduced by complexation to the electron-withdrawing metal center.[60] In both cases, reduction of electron density on the aromatic system leads to weaker aromatic character−in our case antiaromatic character, and in the Stanger case aromatic character.


https://doi.org/10.1021/acs.inorgchem.1c02139
Inorg. Chem. 2021, 60, 14844−14853

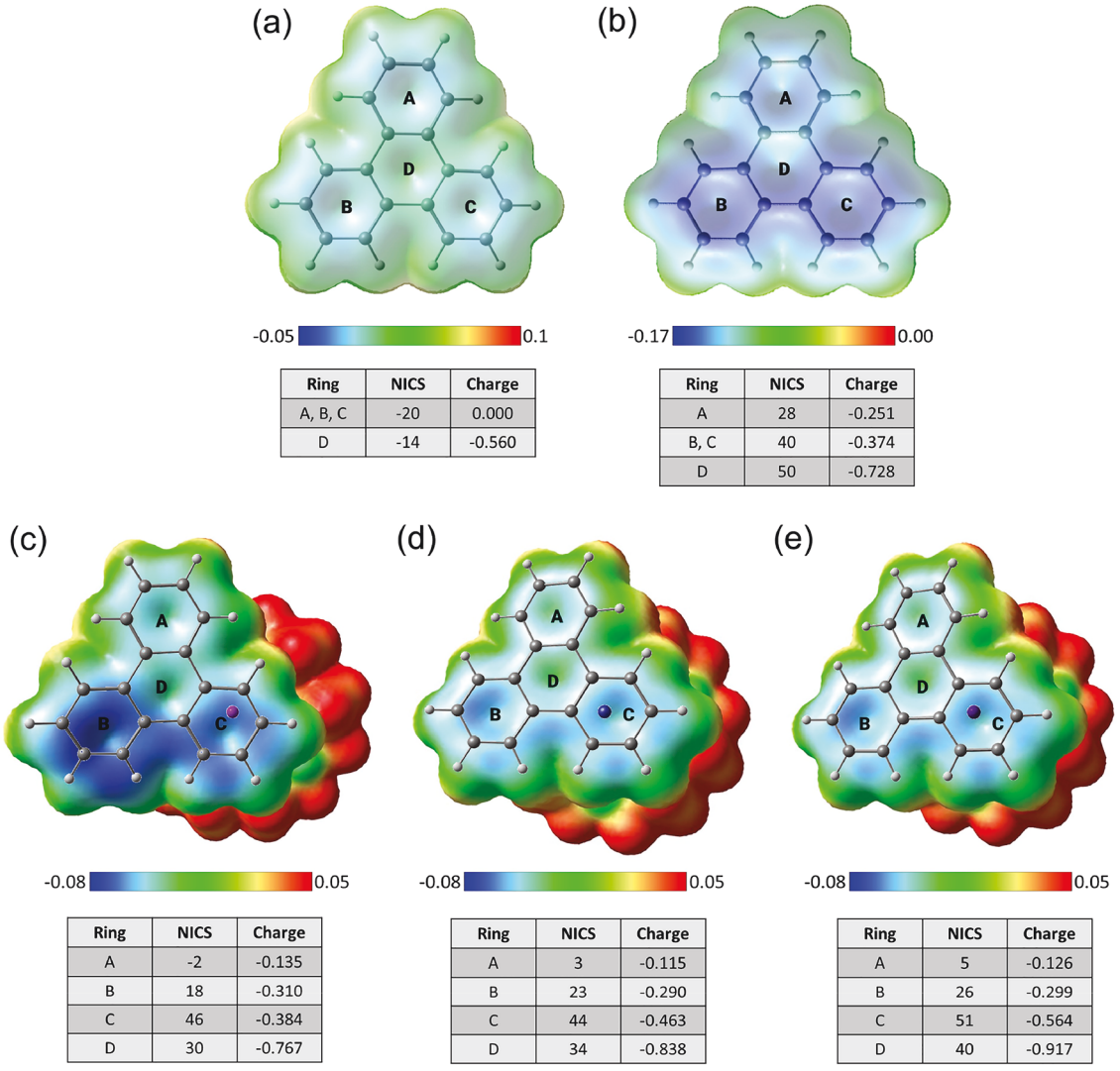


| Ring | NICS | Charge |
|---|---|---|
| A, B, C | -20 | 0.000 |
| D | -14 | -0.560 |

| Ring | NICS | Charge |
|---|---|---|
| A | 28 | -0.251 |
| B, C | 40 | -0.374 |
| D | 50 | -0.728 |

| Ring | NICS | Charge |
|---|---|---|
| A | -2 | -0.135 |
| B | 18 | -0.310 |
| C | 46 | -0.384 |
| D | 30 | -0.767 |

| Ring | NICS | Charge |
|---|---|---|
| A | 3 | -0.115 |
| B | 23 | -0.290 |
| C | 44 | -0.463 |
| D | 34 | -0.838 |

| Ring | NICS | Charge |
|---|---|---|
| A | 5 | -0.126 |
| B | 26 | -0.299 |
| C | 51 | -0.564 |
| D | 40 | -0.917 |

**Figure 6.** Electrostatic potential maps (mapped on the electron density using an isovalue = 0.005 au), NICS(1.7)$_{ZZ}$ (reported in ppm), and Löwdin atomic charges of the systems studied (calculated as the sum of carbon and hydrogen atoms in each ring). For the alkali metal-complexes, the triphenylene is placed on the top, with the metal center behind. The position of the metal relative to the individual rings used in calculations can be seen. The alkali metal ions are mainly complexed to ring C in all structures.

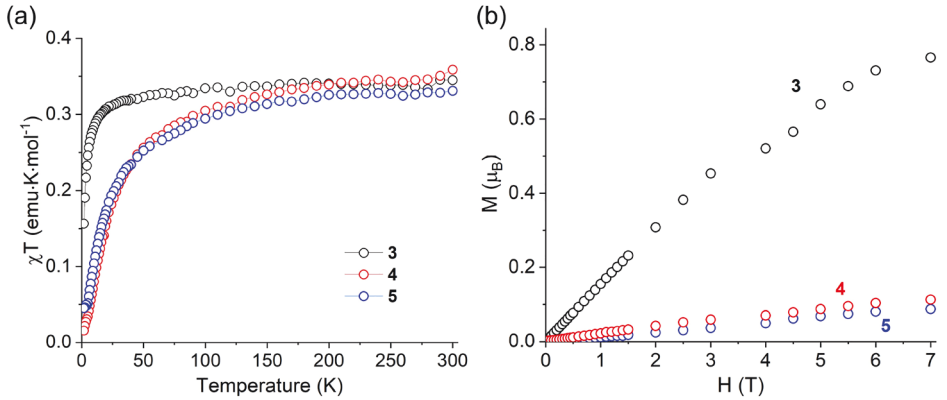


**Figure 7.** Temperature dependence of $\chi T$ at 1000 Oe (a) and field dependence of magnetization at 1.8 K (b) for polycrystalline samples of **3** (black), **4** (red), and **5** (blue).

Overall, the complexation results in $\mathbf{1}^{\cdot-}$ losing a portion of its charge (~17%, ~15%, ~1% for $K^+$, $Rb^+$, and $Cs^+$, respectively) and a notable polarization of the remaining negative charge. This causes a "partitioning" of the $\pi$-system of $\mathbf{1}^{\cdot-}$ into a more negatively charged antiaromatic region and a less negatively charged nonaromatic region. One could interpret this from


https://doi.org/10.1021/acs.inorgchem.1c02139
Inorg. Chem. 2021, 60, 14844−14853

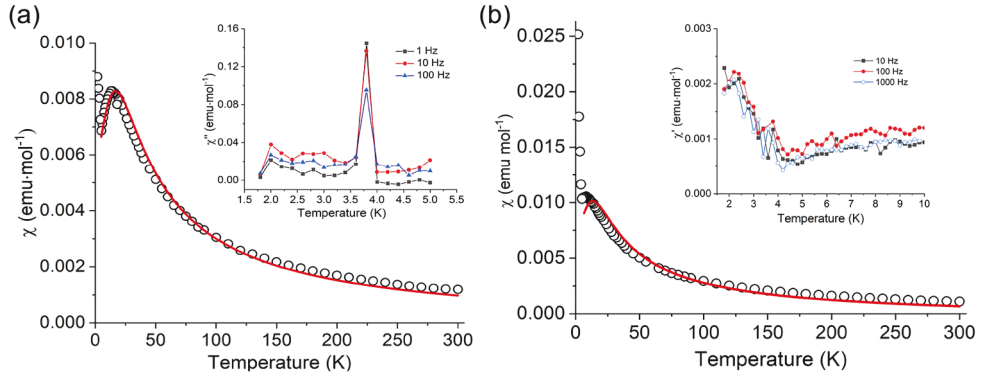


**Figure 8.** Temperature dependence of DC magnetic susceptibility at 1000 Oe for **4** (a) and **5** (b). The solid red lines show the fit to the Bonner–Fisher model. Insets: the temperature dependence of AC magnetic susceptibility for **4** (a) and **5** (b) measured at different frequencies of the applied AC field.

both the aromatic and Coulombic perspectives: the electrostatic interaction with the metal draws the electrons toward one "part" of the triphenylene radical-anion, leading to accumulation of antiaromatic character in that part and reduction of antiaromatic character in the whole system, and mostly in ring A.

**EPR Spectroscopy and Magnetism.** The crystalline samples of **2**–**5** were characterized by X-band EPR spectroscopy, revealing paramagnetic signals with rather broad line widths ($\Delta B$) (Figures S6–S9). The EPR spectrum of **2** exhibits a single resonance with $g$ = 2.00194 and $\Delta B$ = 2.0 G. Similar resonances were observed in the EPR spectra of **3** ($g$ = 2.00635, $\Delta B$ = 2.3 G), **4** ($g$ = 2.00407, $\Delta B$ = 3.7 G), and **5** ($g$ = 2.00150, $\Delta B$ = 2.2 G). The hyperfine splitting could not be resolved due to dipolar broadening in the solid state.

In order to further understand the magnetic behavior and interactions of triphenylene monoanion-radicals $\mathbf{1}^{-}$ in the solid state, DC magnetic susceptibility was measured on polycrystalline samples of **3**, **4**, and **5** under an applied field of 1000 Oe in the 1.8–300 K temperature range. At 300 K, the $\chi T$ values observed for **3**, **4**, and **5** are 0.34, 0.36, and 0.33 emu·K·mol$^{-1}$, respectively (Figure 7a). These values compare well to the value of 0.375 emu·K·mol$^{-1}$ expected for the $S$ = 1/2 system with $g$ = 2.00.

Upon cooling, the $\chi T$ value of **3** remains constant down to 25 K, followed by a sharp decrease to reach a final value of 0.15 emu·K·mol$^{-1}$ at 1.8 K (Figure 7a). The $\chi T$ values of **4** and **5** decrease faster with temperature, reaching, respectively, 0.02 and 0.04 emu·K·mol$^{-1}$ at 1.8 K. The field-dependent magnetization ($M$) measured at 1.8 K showed substantially lower values in the case of **4** and **5** as compared to **3** (Figure 7b). Such behavior suggests stronger antiferromagnetic (AFM) coupling between the $S$ = 1/2 radicals in **4** and **5**. This conclusion is also in agreement with the broader line width observed for the EPR signal of **4** in the solid state, although the EPR line width obtained for **5** is similar to the one observed for **3**. The possible reasons for such behavior will be discussed below. The stronger AFM exchange observed for **4** and **5** can be explained by the closer proximity of the $S$ = 1/2 spins in their crystal structures, where some direct interactions can be observed between the triphenylene radicals (Figure 5b).

The temperature dependence of $\chi$ was featureless for **3** but showed a rounded maximum around 13 K for **4** and around 9 K for **5**, followed by a decrease in the value of $\chi$ and then an abrupt increase at lower temperatures (Figure 8). To examine this behavior more carefully, we performed AC susceptibility measurements which revealed frequency-independent peaks at 3.8 K for **4** and at 2.2 K for **5** (Figure 8, insets), suggesting that these materials undergo AFM ordering at the corresponding temperatures ($T_N$). Thus, samples **4** and **5** show behavior characteristics of a Heisenberg chain of $S$ = 1/2 spins, which is known to exhibit a higher-temperature maximum due to the stronger *intrachain* AFM exchange constant $J$, followed by a lower-temperature AFM ordering due to the weaker *interchain* exchange constant $J'$.[61,62] The lower temperature at which the DC susceptibility peak is observed for **5**, can be explained by the presence of the larger $Cs^+$ cation in the structure of **5**, which leads to the increased separation between the spin centers and lower magnetic ordering temperature (2.2 K for **5** vs 3.8 K for **4**). Such behavior also justifies the larger ERP line width observed for **4** as compared to **5**, which is also in agreement with the weaker AFM exchange interactions in the latter.

To determine the intrachain exchange constant $J$, the magnetic susceptibility curves for **4** and **5** were fit as $\chi(T) = \chi_{1D} + \chi_{TIP}$, where $\chi_{1D}$ is the contribution of the $S$ = 1/2 chains and $\chi_{TIP}$ is the temperature-independent paramagnetism term. The contribution $\chi_{1D}$ is described by the polynomial approximation of the Bonner–Fisher model,[63,64] with the intrachain magnetic exchange Hamiltonian expressed as $\hat{H} = -2J\sum \hat{S}_i\hat{S}_{i+1}$

$$\chi_{1D} = \left[\frac{Ng^2\beta^2}{k_BT}\frac{0.25 - 0.15x + 0.3x^2}{1 - 2x + 0.69x^2 - 6.06x^3}\right] \quad (1)$$

where $x = J/k_BT$, $N$ is Avogadro's number, $\beta$ is Bohr's magneton, $k_B$ is the Boltzmann constant, and $g$ is Lande's $g$-factor. Taking into account that $N\beta^2/k_B \approx 3/8$ and g $\approx$ 2.00 (determined from the EPR measurements), the equation for $\chi(T)$ can be rewritten as

$$\chi = \left[\frac{1.5}{T}\frac{0.25 - 0.15x + 0.3x^2}{1 - 2x + 0.69x^2 - 6.06x^3}\right] + \chi_{TIP} \quad (2)$$

Using eq 2, the temperature dependence of $\chi$ was fit in the range from 300 to 4.2 K for **4** and 300 to 6.2 K for **5**, resulting in the best-fit values of $J = -8.99(1)$ cm$^{-1}$ and $\chi_{TIP} = 2.04(2) \times 10^{-4}$ emu·mol$^{-1}$ for **4** ($R^2$ = 0.9926) and $J = -7.18(8)$ cm$^{-1}$ and $\chi_{TIP} = 5.14(3) \times 10^{-4}$ emu·mol$^{-1}$ for **5** ($R^2$ = 0.9740). The $J$ value for *intrachain* coupling can be used to calculate the effective *interchain* interaction, $J'$, according to the mean-field theory developed by Schulz.[65] Equation 3 defines the


https://doi.org/10.1021/acs.inorgchem.1c02139
Inorg. Chem. 2021, 60, 14844–14853

relationship between the AFM ordering temperature, $T_N$, and the intrachain and interchain exchange constants, $J$ and $J'$

$$J' = -\frac{T_N}{4 \cdot 0.32\sqrt{ln\left(\frac{11.6|J|}{T_N}\right)}} \quad (3)$$

Given $T_N$ = 3.8 K for **4** and $T_N$ = 2.2 K for **5**, as determined from the AC susceptibility data and $J = -8.99(1)$ cm$^{-1}$ and $-7.18(8)$ cm$^{-1}$, respectively, eq 3 results in $J' = -1.63(1)$ cm$^{-1}$ for **4** and $-0.47(6)$ cm$^{-1}$ for **5**. Unfortunately, the lower-temperature maxima characteristic of the AFM ordering could not be observed in our data, although the peaks observed in the AC susceptibility data clearly confirm the magnetic phase transition. Such magnetic phase transitions at low temperatures were also observed for other similar radicals in the solid state. For example, antiferromagnetic ordering at 28.6 K was reported for potassium naphthalenide[66] and, more recently, ferromagnetic ordering at 5.2 K was revealed for potassium 9-phenylanthracene.[67]

## CONCLUSIONS

In the course of chemical reduction study of triphenylene (**1**) with several alkali metals, a series of the triphenylide-based products has been prepared as single-phase crystalline solids. Their successful X-ray structural characterization reveals variations in alkali metal ion binding patterns of the monoreduced triphenylene radical-anion, $\mathbf{1}^{\cdot-}$. While with smaller $Na^+$ ions, the first SSIP product (**2**) has been confirmed, the larger $K^+$, $Rb^+$, and $Cs^+$ ions favored the formation of the CIP complexes (**3**−**5**). The direct structural comparison of the series with the neutral parent reveals a notable geometry perturbation of the triphenylene carbon framework in SSIP, which is further enhanced by direct alkali metal binding in $\pi$-complexes **3**−**5**.

DFT calculations provide further insight into the effects of one-electron acquisition and alkali metal complexation. Notably, the addition of one electron to triphenylene affords an antiaromatic system of lower symmetry with uneven distribution of the negative charge. Subsequent complexation of $\mathbf{1}^{\cdot-}$ stabilizes the system both through attractive electrostatic interaction and through the loss of antiaromaticity due to charge transfer to the metal cation. The extent of charge transfer depends on the metal ion size, going from loss of ∼17% for $K^+$ to only ∼1% for $Cs^+$. The polarization of the remaining charge leads to the formation of two distinct regions in $\mathbf{1}^{\cdot-}$, with the location of greater negative charge corresponding to the location of antiaromatic character (Figure S25). Namely, the more negatively charged region clearly displays paratropic NICS values, while the less negatively charged distant ring is essentially nonaromatic, according to the NICS criterion.

The EPR spectra of **2**−**5** recorded in the solid state show dipolar broadening, which leads to the loss of the hyperfine structure observed in the EPR spectrum of $\mathbf{1}^{\cdot-}$ in solution. The broadening is additionally caused by AFM exchange interactions between $S = 1/2$ radicals, as revealed by magnetic measurements on **3**−**5**. Remarkably, compounds **4** and **5** show magnetic behavior typical of a Heisenberg spin-1/2 chain, wherein a broad maximum is followed by AFM ordering at 3.8 and 2.2 K, respectively. The Bonner−Fisher model was successfully used to fit the susceptibility data in the paramagnetic region. The observation of AFM ordering for **4** and **5** and the lack of such ordering for **3** can be rationalized by the differences in the structural organization of the anionic triphenylene radicals in the $\pi$-complexes with $K^+$, $Rb^+$, and $Cs^+$ counter-cations.

## EXPERIMENTAL SECTION

**Materials and Methods.** All manipulations were carried out using break-and-seal[68] and glovebox techniques under an atmosphere of argon. Tetrahydrofuran (THF) and hexanes were purchased from Sigma-Aldrich, dried over Na/benzophenone, and distilled prior to use. Sodium (99.9%), potassium (98%), rubidium (99.6%), cesium (99.95%), and 18-crown-6 ether (99%) were purchased from Sigma-Aldrich and used as received. As all alkali metals are flammable upon contact with water, they require careful handling under dry Ar atmosphere. Triphenylene ($C_{18}H_{12}$, **1**, Sigma-Aldrich) was purified by sublimation at 175 °C prior to use. The UV−vis spectra were recorded on a Thermo Scientific Evolution 201 UV−visible Spectrophotometer. The X-ray powder diffraction data of **2** were collected on a Bruker D8 Advance diffractometer (Cu K$\alpha$ radiation, focusing Göbel Mirror, LynxEye one-dimensional detector, a step of 0.02° 2$\theta$, 25 °C). The polycrystalline sample under investigation was ground under Ar in the glovebox and placed in the dome-like airtight zero background holder. The X-ray powder diffraction data of were collected on a Bruker D8 VENTURE diffractometer (Cu INCOATEC I$\mu$S microfocus X-ray K$\alpha$ radiation, mirror monochromator, PHOTON 100 CMOS area detector, a step of 10° 2$\theta$, 300 s per step, 173.15 °C). The crystalline samples under investigation were ground under Ar in the glovebox and mounted on the MiTeGen dual thickness MicroMounts sample holder (30 $\mu$m). LeBail fit for powder diffraction patterns was performed using TOPAS, version 4 software package (Bruker AXS, 2006). Electron paramagnetic resonance (EPR) for solution sample of **2** was collected with a Bruker ER-200D-SRC X-band spectrometer interfaced to a Compaq 386 PC equipped with an IBM analog-to-digital converter and Scientific Software Services Systems (Bloomington, IL). EPR measurements on solid samples of **2**−**5** were performed at room temperature at the X-band frequency (9.86 GHz), using a Bruker EleXsys E500 ESR spectrometer equipped with an ER 049X microwave bridge. $\alpha,\alpha'$-Diphenyl-$\beta$-picryl hydrazyl (DPPH) was used as a reference standard. Magnetic properties were measured on polycrystalline samples of **3**−**5**, using a magnetic property measurement system (MPMS-XL, Quantum Design) equipped with a superconducting quantum interference device (SQUID). Magnetic susceptibility was measured in an applied direct-current (DC) magnetic field of 1000 Oe in the 1.8−300 K temperature range. The field-dependent magnetization was measured at 1.8 K with the applied field varying from 0 to 7 T. The alternating-current (AC) susceptibility measurements were performed in the range from 1.8 to 15 K, under zero DC field. The amplitude of the AC field was set at 5 Oe, and the field frequency was varied from 1 to 1000 Hz. The data were corrected for independently measured diamagnetic background from the sample holder.

*Preparation of [{Na$^+$(18-crown-6)(THF)$_2$}($\mathbf{1}^{\cdot-}$)] (**2**).* THF (1.5 mL) was added into a customized glass system containing excess Na (10.0 mg, 0.44 mmol), **1** (5.0 mg, 0.02 mmol), and 18-crown-6 (5.5 mg, 0.02 mmol). The reaction mixture was allowed to stir under argon at 25 °C for 20 h. The initial off-white color of the solution turned to dark violet after 12 min and remained the same until the reaction was stopped. The mixture was filtered, and the dark violet filtrate was layered with 1.0 mL of anhydrous hexanes. The ampule was sealed and stored at 5 °C. After 5 days, black needle-shaped crystals were present in good yield. Yield: 9.5 mg, 70%. UV−vis ($\lambda$, nm): 414, 544, 686, 757.

*Preparation of [{K$^+$(18-crown-6)}($\mathbf{1}^{\cdot-}$)]$_\infty$ (**3**).* THF (1.5 mL) was added into a customized glass system containing excess K (10.0 mg, 0.26 mmol), **1** (5.0 mg, 0.02 mmol), and 18-crown-6 (5.5 mg, 0.02 mmol). The reaction mixture was allowed to stir under argon at 25 °C for 2 h. The initial off-white color of the solution turned to dark violet after 8 min and remained the same until the reaction was stopped.


https://doi.org/10.1021/acs.inorgchem.1c02139
Inorg. Chem. 2021, 60, 14844−14853

The mixture was filtered, and the dark violet filtrate was layered with 1.0 mL of anhydrous hexanes. The ampule was sealed and stored at 5 °C. After 5 days, black needle-shaped crystals were present in moderate yield. Yield: 6.4 mg, 55%. UV−vis ($\lambda$, nm): 413, 540, 682, 751.

*Preparation of [{Rb$^+$(18-crown-6)}(**1**$^{\bullet-}$)] (**4**).* THF (1.5 mL) was added into a customized glass system containing excess Rb (15.0 mg, 0.18 mmol), **1** (5.0 mg, 0.02 mmol), and 18-crown-6 (5.5 mg, 0.02 mmol). The reaction mixture was allowed to stir under argon at 25 °C for 2 h. The initial off-white color of the solution turned to dark violet after 5 min and remained the same until the reaction was stopped. The mixture was filtered, and the dark violet filtrate was layered with 1.0 mL of anhydrous hexanes. The ampule was sealed and stored at 5 °C. After 5 days, black needle-shaped crystals were present in moderate yield. Yield: 7.6 mg, 60%. UV−vis ($\lambda$, nm): 412, 534, 678, 748.

*Preparation of [{Cs$^+$(18-crown-6)}(**1**$^{\bullet-}$)] (**5**).* THF (1.5 mL) was added into a customized glass system containing excess Cs (10.0 mg, 0.08 mmol), **1** (5.0 mg, 0.02 mmol), and 18-crown-6 (5.5 mg, 0.02 mmol). The reaction mixture was allowed to stir under argon at 25 °C for 15 min. The initial off-white color of the solution turned to dark violet after 5 min and remained the same until the reaction was stopped. The mixture was filtered, and the dark violet filtrate was layered with 1.2 mL of anhydrous hexanes. The ampule was sealed and stored at 5 °C. After 2 days, black needle-shaped crystals were present in moderate yield. Yield: 8.9 mg, 65%. UV−vis ($\lambda$, nm): 410, 534, 678, 748.

**Crystal Structure Determination and Refinement.** Data collections of **2**−**5** were performed on a Bruker VENTURE system equipped with a PHOTON 100 CMOS detector, a Mo-target fine-focus X-ray source ($\lambda$ = 0.71073 Å), and a graphite monochromator. All data were collected at 100 K crystal temperature (Oxford Cryosystems CRYOSTREAM 700), 50 kV and 30 mA with an appropriate 0.5° $\omega$ and $\varphi$ scan strategy. Data reduction and integration were performed with SAINT (version 8.37A).[69] Data were corrected for absorption effects using the empirical methods as implemented in SADABS (version 2016/2).[70] The structures were solved by SHELXT (version 2018/2)[71] and refined by full-matrix least-squares procedures using the SHELXL program (version 2018/3)[72] through the OLEX2[73] graphical interface. All non-hydrogen atoms, including those in disordered parts, were refined anisotropically. All H atoms were included at calculated positions and refined as riders, with $U_{iso}$(H) = 1.2 $U_{eq}$(C). More crystallographic and structure refinement details (Table S5), as well as ORTEP drawings and solid-state packing, are shown in the Supporting Information.

## ■ ASSOCIATED CONTENT

### Supporting Information

The Supporting Information is available free of charge at https://pubs.acs.org/doi/10.1021/acs.inorgchem.1c02139.

X-ray structural details, UV−vis and EPR spectroscopic data, and computational details (PDF)

### Accession Codes

CCDC 2096345 (**2**), 2096346 (**3**), 2096347 (**4**), and 2096348 (**5**) contain the supplementary crystallographic data for this paper. These data can be obtained free of charge from the Cambridge Crystallographic Data Centre via www.ccdc.cam.ac.uk/data_request/cif.

## ■ AUTHOR INFORMATION


### Corresponding Authors

**Marina A. Petrukhina** − *Department of Chemistry, University at Albany, State University of New York, Albany, New York 12222, United States;* orcid.org/0000-0003-0221-7900; Email: mpetrukhina@albany.edu

**Michael Shatruk** − *Department of Chemistry and Biochemistry, Florida State University, Tallahassee, Florida 32306-4390, United States;* orcid.org/0000-0002-2883-4694; Email: shatruk@chem.fsu.edu

**Renana Gershoni-Poranne** − *Laboratorium für Organische Chemie, ETH Zürich, CH-8093 Zürich, Switzerland; Schulich Faculty of Chemistry, Technion − Israel Institute of Technology, Haifa 3200008, Israel;* orcid.org/0000-0002-2233-6854; Email: renana.poranne@org.chem.ethz.ch

### Authors

**Zheng Zhou** − *Department of Chemistry, University at Albany, State University of New York, Albany, New York 12222, United States*

**Ökten Üngör** − *Department of Chemistry and Biochemistry, Florida State University, Tallahassee, Florida 32306-4390, United States*

**Zheng Wei** − *Department of Chemistry, University at Albany, State University of New York, Albany, New York 12222, United States*

**Alexandra Tsybizova** − *Laboratorium für Organische Chemie, ETH Zürich, CH-8093 Zürich, Switzerland*

Complete contact information is available at: https://pubs.acs.org/10.1021/acs.inorgchem.1c02139


### Notes

The authors declare no competing financial interest.

## ■ ACKNOWLEDGMENTS

Financial support of this work from the U.S. National Science Foundation (CHE-2003411 to M.A.P. and CHE-1955754 to M.S.) is gratefully acknowledged. We also thank Dr. Vladimir M. Grigoryants at the University at Albany for the EPR solution measurement and Prof. Joseph Zadrozny from Colorado State University for providing access to the MPMS for measurements on compound **5**. This research also used resources provided by the Materials Characterization Laboratory (FSU075000MAC) at the FSU Department of Chemistry and Biochemistry. A.T. and R.G.P. express their thanks to Eno Paenurk for fruitful discussions and to Prof. Peter Chen for his scientific and financial support and for access to the computational resources at ETH Zurich. R.G.P. is a Branco Weiss Fellow and a Career Advancement Fellow.

## ■ REFERENCES


(1) Benshafrut, R.; Shabtai, E.; Rabinovitz, M.; Scott, L. T. $\pi$-Conjugated Anions: From Carbon-Rich Anions to Charged Carbon Allotropes. *Eur. J. Org. Chem.* **2000**, *2000*, 1091−1106.

(2) Sternfeld, T.; Rabinovitz, M. In *Carbon-Rich Compounds*; Haley, M. M., Tykwinski, R. R., Ed.; Wiley: Weinheim, Germany, 2006; pp 566−623.

(3) Eisenberg, D.; Shenhar, R.; Rabinovitz, M. In *Fragments of Fullerenes and Carbon Nanotubes: Designed Synthesis, Unusual Reactions, and Coordination Chemistry*; Petrukhina, M. A.; Scott, L. T., Ed.; Wiley: Hoboken, NJ, 2012; pp 63−93.

(4) Eisenberg, D.; Shenhar, R. Polyarene Anions: Interplay between Theory and Experiment. *WIREs: Comput. Mol. Sci.* **2012**, *2*, 525−547.

(5) Tzirakis, M. D.; Orfanopoulos, M. Radical Reactions of Fullerenes: From Synthetic Organic Chemistry to Materials Science and Biology. *Chem. Rev.* **2013**, *113*, 5262−5321.

(6) Zabula, A. V.; Petrukhina, M. A. Structural Perspective on Aggregation of Alkali Metal Ions with Charged Planar and Curved Carbon $\pi$-Surfaces. *Adv. Organomet. Chem.* **2013**, *61*, 375−462.

(7) Bock, H.; Gharagozloo-Hubmann, K.; Sievert, M.; Prisner, T.; Havlas, Z. Single Crystals of an Ionic Anthracene Aggregate with a Triplet Ground State. *Nature* **2000**, *404*, 267−269.
(8) Ayalon, A.; Sygula, A.; Cheng, P.-C.; Rabinovitz, M.; Rabideau, P. W.; Scott, L. T. Stable High-Order Molecular Sandwiches: Hydrocarbon Polyanion Pairs with Multiple Lithium Ions Inside and Out. *Science* **1994**, *265*, 1065−1067.
(9) Treitel, N.; Sheradsky, T.; Peng, L.; Scott, L. T.; Rabinovitz, M. $C_{30}H_{12}^{6-}$: Self-Aggregation, High Charge Density, and Pyramidalization in a Supramolecular Structure of a Supercharged Hemifullerene. *Angew. Chem., Int. Ed.* **2006**, *45*, 3273−3277.
(10) Eisenberg, D.; Jackson, E. A.; Quimby, J. M.; Scott, L. T.; Shenhar, R. The Bicorannulenyl Dianion: A Charged Overcrowded Ethylene. *Angew. Chem., Int. Ed.* **2010**, *49*, 7538−7542.
(11) Wombacher, T.; Goddard, R.; Lehmann, C. W.; Schneider, J. J. Complete Charge Separation Provoked by Full Cation Encapsulation in the Radical Mono- and Di-anions of 5,6:11,12-di-*o*-Phenylenetetracene. *Dalton Trans.* **2018**, *47*, 10874−10883.
(12) Zabula, A. V.; Filatov, A. S.; Spisak, S. N.; Rogachev, A. Yu.; Petrukhina, M. A. A Main Group Metal Sandwich: Five Lithium Cations Jammed Between Two Corannulene Tetraanion Decks. *Science* **2011**, *333*, 1008−1011.
(13) Zabula, A. V.; Filatov, A. S.; Xia, J.; Jasti, R.; Petrukhina, M. A. Tightening of the Nanobelt upon Multielectron Reduction. *Angew. Chem., Int. Ed.* **2013**, *52*, 5033−5036.
(14) Spisak, S. N.; Wei, Z.; O'Neil, N. J.; Rogachev, A. Yu.; Amaya, T.; Hirao, T.; Petrukhina, M. A. Convex and Concave Encapsulation of Multiple Potassium Ions by Sumanenyl Anions. *J. Am. Chem. Soc.* **2015**, *137*, 9768−9771.
(15) Zabula, A. V.; Spisak, S. N.; Filatov, A. S.; Rogachev, A. Yu.; Petrukhina, M. A. Record Alkali Metal Intercalation by Highly Charged Corannulene. *Acc. Chem. Res.* **2018**, *51*, 1541−1549.
(16) Zhou, Z.; Spisak, S. N.; Xu, Q.; Rogachev, A. Yu.; Wei, Z.; Marcaccio, M.; Petrukhina, M. A. Fusing a Planar Group to a $\pi$-Bowl: Electronic and Molecular Structure, Aromaticity and Solid-State Packing of Naphthocorannulene and its Anions. *Chem. - Eur. J.* **2018**, *24*, 3455−3463.
(17) Spisak, S. N.; Bühringer, M. U.; Wei, Z.; Zhou, Z.; Tykwinski, R. R.; Petrukhina, M. A. Structural and Electronic Effects of Stepwise Reduction of a Tetraaryl[3]Cumulene. *Angew. Chem., Int. Ed.* **2019**, *58*, 2023−2028.
(18) Zhou, Z.; Wei, Z.; Tokimaru, Y.; Ito, S.; Nozaki, K.; Petrukhina, M. A. Stepwise Reduction of Azapentabenzocorannulene. *Angew. Chem., Int. Ed.* **2019**, *58*, 12107−12111.
(19) Zhou, Z.; Wang, X.-Y.; Wei, Z.; Müllen, K.; Petrukhina, M. A. Charging OBO-Fused Double [5]Helicene with Electrons. *Angew. Chem., Int. Ed.* **2019**, *58*, 14969−14973.
(20) Bock, H.; Havlas, Z.; Gharagozloo-Hubmann, K.; Sievert, M. The $Li^+$-Initiated Twofold Dehydrogenation and C−C Bond Formation of Hexaphenylbenzene to the Dilithium Salt of the 9,10-Diphenyltetrabenz[*a*,*c*,*h*,*j*]anthracene Dianion. *Angew. Chem., Int. Ed.* **1999**, *38*, 2240−2243.
(21) Bock, H.; Sievert, M.; Bogdan, C. L.; Kolbesen, B. O.; Wittershagen, A. Biphenylene Ring Expansion by a $(H_3C)_2Si$ Link from Silicone Grease As Proven by the Crystal Structures of [(Sodium$^+$[2.2.1]cryptand)(9,9-dimethylsilafluorene$^{\bullet-}$)] as Well as [Sodium$^+$(triglyme)$_2$(biphenylene$^{\bullet-}$)] and by Total-Reflection X-ray Fluorescence Spectrometry (TXRF)[1]. *Organometallics* **1999**, *18*, 2387−2389.
(22) Zhou, Z.; Kawade, R. K.; Wei, Z.; Kuriakose, F.; Üngör, Ö.; Jo, M.; Shatruk, M.; Gershoni-Poranne, R.; Petrukhina, M. A.; Alabugin, I. V. Negative Charge as a Lens for Concentrating Antiaromaticity: Using a Pentagonal "Defect" and Helicene Strain for Cyclizations. *Angew. Chem., Int. Ed.* **2020**, *59*, 1256−1262.
(23) Aprahamian, I.; Hoffman, R. E.; Sheradsky, T.; Preda, D. V.; Bancu, M.; Scott, L. T.; Rabinovitz, M. A Four-Step Alternating Reductive Dimerization/Bond Cleavage of Indenocorannulene. *Angew. Chem., Int. Ed.* **2002**, *41*, 1712−1715.
(24) Aprahamian, I.; Preda, D. V.; Bancu, M.; Belanger, A. P.; Sheradsky, T.; Scott, L. T.; Rabinovitz, M. Reduction of Bowl-Shaped Hydrocarbons: Dianions and Tetraanions of Annelated Corannulenes. *J. Org. Chem.* **2006**, *71*, 290−298.
(25) Spisak, S. N.; Zabula, A. V.; Alkan, M.; Filatov, A. S.; Rogachev, A. Yu.; Petrukhina, M. A. Site-Directed Dimerization of Bowl-Shaped Radical Anions to Form a $\sigma$-Bonded Dibenzocorannulene Dimer. *Angew. Chem., Int. Ed.* **2018**, *57*, 6171−6175.
(26) Rogachev, A. Yu.; Alkan, M.; Li, J.; Liu, S.; Spisak, S. N.; Filatov, A. S.; Petrukhina, M. A. Mono-reduced Corannulene: To Couple and Not to Couple in One Crystal. *Chem. - Eur. J.* **2019**, *25*, 14140−14147.
(27) Garst, J. F. Electron Transfer, Naphthalene Radical Anion, and Alkyl Halides. *Acc. Chem. Res.* **1971**, *4*, 400−406.
(28) García-Gallastegui, A.; Obieta, I.; Bustero, I.; Imbuluzqueta, G.; Arbiol, J.; Miranda, J. I.; Aizpurua, J. M. Reductive Functionalization of Single-Walled Carbon Nanotubes with Lithium Metal Catalyzed by Electron Carrier Additives. *Chem. Mater.* **2008**, *20*, 4433−4438.
(29) Manzetti, S. In *Handbook of Polycyclic Aromatic Hydrocarbons*; Bandeira, G. C., Meneses, H. E., Ed.; Nova Science: 2011; pp 423−435.
(30) Wang, S.; Yata, S.; Nagano, J.; Okano, Y.; Kinoshita, H.; Kikuta, H.; Yamabe, T. A New Carbonaceous Material with Large Capacity and High Efficiency for Rechargeable Li-Ion Batteries. *J. Electrochem. Soc.* **2000**, *147*, 2498.
(31) Friedlein, R.; Crispin, X.; Salaneck, W. R. Molecular Parameters Controlling the Energy Storage Capability of Lithium Polyaromatic Hydrocarbon Intercalation Compounds. *J. Power Sources* **2004**, *129*, 29−33.
(32) Grimsdale, A. C.; Wu, J.; Müllen, K. New Carbon-Rich Materials for Electronics, Lithium Battery, and Hydrogen Storage Applications. *Chem. Commun.* **2005**, 2197−2204.
(33) Bachman, J. C.; Kavian, R.; Graham, D. J.; Kim, D. Y.; Noda, S.; Nocera, D. G.; Shao-Horn, Y.; Lee, S. W. Electrochemical Polymerization of Pyrene Derivatives on Functionalized Carbon Nanotubes for Pseudocapacitive Electrodes. *Nat. Commun.* **2015**, *6*, 7040.
(34) Sato, S.; Unemoto, A.; Ikeda, T.; Orimo, S.-i.; Isobe, H. Carbon-Rich Active Materials with Macrocyclic Nanochannels for High-Capacity Negative Electrodes in All-Solid-State Lithium Rechargeable Batteries. *Small* **2016**, *12*, 3381−3387.
(35) Rodríguez-Pérez, I. A.; Bommier, C.; Fuller, D. D.; Leonard, D. P.; Williams, A. G.; Ji, X. Toward Higher Capacities of Hydrocarbon Cathodes in Dual-Ion Batteries. *ACS Appl. Mater. Interfaces* **2018**, *10*, 43311−43315.
(36) He, D.; Xiao, F.; Wang, Z.; He, A.; Liu, R.; Jin, G. Dynamic Hierarchical Self-Assemble Small Molecule Structure Hexabenzocoronene for the High-Performance Anodes Lithium Ion Storage. *Nanoscale Res. Lett.* **2019**, *14*, 65.
(37) Mitsuhashi, R.; Suzuki, Y.; Yamanari, Y.; Mitamura, H.; Kambe, T.; Ikeda, N.; Okamoto, H.; Fujiwara, A.; Yamaji, M.; Kawasaki, N.; Maniwa, Y.; Kubozono, Y. Superconductivity in Alkali-Metal-Doped Picene. *Nature* **2010**, *464*, 76−79.
(38) Takabayashi, Y.; Menelaou, M.; Tamura, H.; Takemori, N.; Koretsune, T.; Štefančič, A.; Klupp, G.; Buurma, A. J. C.; Nomura, Y.; Arita, R.; Arčon, D.; Rosseinsky, M. J.; Prassides, K. $\pi$-Electron S = 1/2 Quantum Spin-Liquid State in an Ionic Polyaromatic Hydrocarbon. *Nat. Chem.* **2017**, *9*, 635−643.
(39) Paul, D. E.; Lipkin, D.; Weissman, S. I. Reaction of Sodium Metal with Aromatic Hydrocarbons[1,2]. *J. Am. Chem. Soc.* **1956**, *78*, 116−120.
(40) Arick, M. R.; Van Broekhoven, J. A. M.; Pijpers, F. W.; De Boer, E. Optical Studies of Triphenylene Anion. *J. Am. Chem. Soc.* **1972**, *94*, 7531−7536.
(41) Lemaire, O.; De Backer, M.; Devos, A.; Sauvage, F. X. A Study of Alkali Metal Triphenylides in the Solid State. *Synth. Met.* **2001**, *123*, 61−68.


https://doi.org/10.1021/acs.inorgchem.1c02139
*Inorg. Chem.* 2021, 60, 14844−14853

(42) Rieger, R.; Müllen, K. Forever Young: Polycyclic Aromatic Hydrocarbons as Model Cases for Structural and Optical Studies. *J. Phys. Org. Chem.* **2010**, *23*, 315−325.
(43) Zhao, X.-M.; Zhong, G.-H.; Zhang, J.; Huang, Q.-W.; Goncharov, A. F.; Lin, H.-Q.; Chen, X.-J. Combined Experimental and Computational Study of High-Pressure Behavior of Triphenylene. *Sci. Rep.* **2016**, *6*, 25600.
(44) Koning, R. E.; Zandvoort, H.; Zandstra, P. J. MCD of the Triphenylene Anion Radical. Influence of Ion-Pairing and Jahn-Teller Effect. *Chem. Phys.* **1978**, *28*, 343−355.
(45) Meerholz, K.; Heinze, J. Multiple Reversible Electrochemical Reduction of Aromatic Hydrocarbons in Liquid Alkylamines. *J. Am. Chem. Soc.* **1989**, *111*, 2325−2326.
(46) Devos, A.; Lannoo, M. Electron-Phonon Coupling for Aromatic Molecular Crystals: Possible Consequences for Their Superconductivity. *Phys. Rev. B: Condens. Matter Mater. Phys.* **1998**, *58*, 8236−8239.
(47) Hatanaka, M. Pseudo Jahn−Teller Effects of Triphenylene Dianion. *J. Mol. Struct.: THEOCHEM* **2009**, *915*, 69−72.
(48) van Willigen, H.; van Broekhoven, J. A. M.; de Boer, E. An E.S.R. Study of the Mono and Dinegative Ions of Triphenylene. Evidence for the Jahn-Teller Instability of the Triplet Dianion. *Mol. Phys.* **1967**, *12*, 533−548.
(49) Stephen, M. R. D.; Wagner, B.; Freed, J. H. ESR Relaxation Studies on Orbitally Degenerate Free Radicals. II. *J. Chem. Phys.* **1970**, *52*, 5404−5417.
(50) Štefančič, A.; Klupp, G.; Knaflič, T.; Yufit, D. S.; Tavčar, G.; Potočnik, A.; Beeby, A.; Arčon, D. Triphenylide-Based Molecular Solid—A New Candidate for a Quantum Spin-Liquid Compound. *J. Phys. Chem. C* **2017**, *121*, 14864−14871.
(51) Ahmed, F. R.; Trotter, J. The Crystal Structure of Triphenylene. *Acta Crystallogr.* **1963**, *16*, 503−508.
(52) Prasad, P. R.; Singh, H. B.; Butcher, R. J. Isolation and Structures of Some Selenium and Tellurium Derivatives of 1, 4, 5, 8, 9, 12-Hexabromododecahydrotriphenylene as Co-Crystals of Triphenylene. *J. Chem. Sci.* **2014**, *126*, 1311−1321.
(53) Zabula, A. V.; Spisak, S. N.; Filatov, A. S.; Petrukhina, M. A. Self-Assembly of Charged Supramolecular Sandwiches Formed by Corannulene Tetraanions and Lithium Cations. *Organometallics* **2012**, *31*, 5541−5545.
(54) Spisak, S. N.; Sumner, N. J.; Zabula, A. V.; Filatov, A. S.; Rogachev, A. Yu.; Petrukhina, M. A. Tuning Binding of Rubidium Ions to Planar and Curved Negatively Charged $\pi$ Surfaces. *Organometallics* **2013**, *32*, 3773−3779.
(55) Schleyer, P. v. R.; Maerker, C.; Dransfeld, A.; Jiao, H.; van Eikema Hommes, N. J. R. Nucleus-Independent Chemical Shifts: A Simple and Efficient Aromaticity Probe. *J. Am. Chem. Soc.* **1996**, *118*, 6317−6318.
(56) Gershoni-Poranne, R.; Stanger, A. Magnetic Criteria of Aromaticity. *Chem. Soc. Rev.* **2015**, *44*, 6597−6615.
(57) Stanger, A. NICS - Past and Present. *Eur. J. Org. Chem.* **2020**, *2020*, 3120−3127.
(58) Steiner, E.; Fowler, P. W. Four- and Two-Electron Rules for Diatropic and Paratropic Ring Currents in Monocyclic $\pi$ Systems. *Chem. Commun.* **2001**, 2220−2221.
(59) Steiner, E.; Fowler, P. W. Patterns of Ring Currents in Conjugated Molecules: A Few-Electron Model Based on Orbital Contributions. *J. Phys. Chem. A* **2001**, *105*, 9553−9562.
(60) Stanger, A. Is (Benzene)Cr(CO)3 Really More Aromatic Than Benzene? *Can. J. Chem.* **2017**, *95*, 263−270.
(61) Mikeska, H.-J.; Kolezhuk, A. K. One-Dimensional Magnetism. *Lect. Notes Phys.* **2004**, *645*, 1−83.
(62) Richter, J.; Schulenburg, J.; Honecker, A. Quantum Magnetism in Two Dimensions: From Semi-Classical Néel Order to Magnetic Disorder. *Lect. Notes Phys.* **2004**, *645*, 85−153.
(63) Bonner, J. C.; Fisher, M. E. Linear Magnetic Chains with Anisotropic Coupling. *Phys. Rev.* **1964**, *135*, A640−A658.
(64) Savina, Y.; Bludov, O.; Pashchenko, V.; Gnatchenko, S. L.; Lemmens, P.; Berger, H. Magnetic Properties of the Antiferromagnetic Spin-1/2 Chain System $\beta$-$TeVO_4$. *Phys. Rev. B: Condens. Matter Mater. Phys.* **2011**, *84*, 104447.
(65) Schulz, H. J. Dynamics of Coupled Quantum Spin Chains. *Phys. Rev. Lett.* **1996**, *77*, 2790−2793.
(66) Scott, T. A.; Ooro, B. A.; Collins, D. J.; Shatruk, M.; Yakovenko, A.; Dunbar, K. R.; Zhou, H.-C. After 118 Years, the Isolation of Two Common Radical Anion Reductants as Simple, Stable Solids. *Chem. Commun.* **2009**, 65−67.
(67) Fu, M.-A.; Wang, R.-S.; Yang, H.; Zhang, P.-Y.; Zhang, C.-F.; Chen, X.-J.; Gao, Y.; Huang, Z.-B. $\pi$-Electron Weak Ferromagnetism in Potassium-Intercalated 9-Phenylanthracene. *Carbon* **2021**, *173*, 587−593.
(68) Kozhemyakina, N. V.; Nuss, J.; Jansen, M. Demonstration of the "Break-and-Seal" Approach to Fullerides of Complex Cations at the Example of $KC_{60}(THF)_5 \cdot 2THF$. *Z. Anorg. Allg. Chem.* **2009**, *635*, 1355−1361.
(69) SAINT; part of Bruker APEX3 software package (version 2017.3−0): Bruker AXS. 2017,.
(70) SADABS; part of Bruker APEX3 software package (version 2017.3−0): Bruker AXS. 2017,.
(71) Sheldrick, G. M. SHELXT - Integrated Space-Group and Crystal-Structure Determination. *Acta Crystallogr., Sect. A: Found. Adv.* **2015**, *A71*, 3−8.
(72) Sheldrick, G. M. Crystal Structure Refinement with SHELXL. *Acta Crystallogr., Sect. C: Struct. Chem.* **2015**, *C71*, 3−8.
(73) Dolomanov, O. V.; Bourhis, L. J.; Gildea, R. J.; Howard, J. A. K.; Puschmann, H. OLEX2: A Complete Structure Solution, Refinement and Analysis Program. *J. Appl. Crystallogr.* **2009**, *42*, 339−341.


https://doi.org/10.1021/acs.inorgchem.1c02139
*Inorg. Chem.* 2021, 60, 14844−14853